Local Chromatin Organization and Net Charge Modulate DNA Glycosylase Efficiency in Live Cells

Limin Xiang

limin.xiang@whu.edu.cn

Wuhan University https://orcid.org/0000-0003-1488-2705

Jingfang Zhao

Wuhan University

Jingwen Deng

Wuhan University

Zhe Zhao

University of Muenster https://orcid.org/0000-0002-1819-5518

Quan Yuan

Wuhan University

Weihua Huang

Wuhan University https://orcid.org/0000-0001-8951-075X

Li-Sheng Zhang

HKUST https://orcid.org/0000-0003-1872-9978

Shuoxing Jiang

Nanjing University

Miao Yu

Wuhan University

Guohong Li

Wuhan University

Ke Xu

University of California, Berkeley https://orcid.org/0000-0002-2788-194X

Article

Keywords:

Posted Date: October 22nd, 2025

DOI: https://doi.org/10.21203/rs.3.rs-6816177/v1

Additional Declarations: There is **NO** Competing Interest.

Local Chromatin Organization and Net Charge Modulate DNA Glycosylase Efficiency in Live Cells

Jingfang Zhao[1], Jingwen Deng[1], Zhe Zhao[1,6], Quan Yuan[2], Weihua Huang[2], Li-Sheng Zhang[4], Shuoxing Jiang[5], Miao Yu[3], Guohong Li[3], Ke Xu[7], Limin Xiang[1]*

1. College of Chemistry and Molecular Sciences, State Key Laboratory of Metabolism and Regulation in Complex Organisms, College of Life Sciences, Taikang Center for Life and Medical Sciences, Wuhan University, Wuhan, China 430072

2. College of Chemistry and Molecular Sciences, Wuhan University, Wuhan, China 430072

3. State Key Laboratory of Metabolism and Regulation in Complex Organisms, College of Life Sciences, Taikang Center for Life and Medical Sciences, Wuhan University, Wuhan, China 430072

4. Department of Chemistry and Division of Life Science, The Hong Kong University of Science and Technology (HKUST), Kowloon 999077 Hong Kong SAR, China

5. State Key Laboratory of Coordination Chemistry, Department of Biomedical Engineering, College of Engineering and Applied Sciences, Nanjing University, Nanjing, Jiangsu 210023, P. R. China

6. Department of Physics, University of Muenster, Muenster, 48159, Germany

7. Department of Chemistry, University of California, Berkeley, California, United States 94720

*Corresponding author. limin.xiang@whu.edu.cn

Abstract: Diffusion governs molecular encounter rates and underpins the efficiency of chemical reactions, including those catalyzed by enzymes in crowded cellular environments. In the context of DNA repair, how local nuclear organization modulates enzymatic search efficiency remains poorly understood. Here, we apply spatially resolved single-molecule diffusivity mapping to investigate the dynamics of human 8-oxoguanine DNA glycosylase (hOGG1) in live cell nuclei. We identify three key determinants of enzymatic performance: chromatin compactness, the

balance between one-dimensional sliding and three-dimensional hopping, and the 3D diffusion rate during hopping. Approximately 50% of the search process occurs via sliding along chromatin, and a small-molecule activator enhances repair efficiency by inducing chromatin condensation. Guided by theoretical modeling, we further show that reducing the enzyme's net positive charge increases hopping mobility and improves repair efficiency. These findings demonstrate how chromatin architecture and electrostatic properties govern enzyme dynamics *in vivo*, offering a general strategy for tuning intracellular reactivity through physicochemical design.

Introduction:

Diffusion rate is a ubiquitous factor that determines chemical reaction rates. While in a beaker, all reactants exhibit uniform diffusion rates, the scenario shifts in cellular systems where biomolecules encounter a heterogeneous environment that complicates their diffusion. Macromolecular crowding within cells significantly hinders long-distance diffusion, reducing collision frequencies[1]. Moreover, the presence of myriad non-targeted species in the surroundings fosters non-specific interactions with reactants, further slow reaction rates. These challenges raise the central question of how enzymes efficiently locate their targets in the crowded and heterogeneous nuclear environment, akin to solving a needle-in-the-haystack puzzle.

The challenge intensifies for DNA repair enzymes tasked with locating rare damaged sites promptly among billions of base pairs on chromatin[2]. For instance, DNA glycosylase, a member of the DNA repair enzyme family, a key player in base-excision DNA repair, exemplifies this by catalyzing the removal of damaged bases, which often differ from normal bases by only a few atomic positions[3]. To overcome this, enzymes employ a ′facilitated diffusion′ process, rapidly scanning non-target DNA before specifically binding to damaged sites[4]. This combination of one-dimensional diffusion along DNA strands and three-dimensional diffusion in DNA-free regions broadly defines the diffusive behavior of DNA glycosylases in cells.

Recent advancements in microscopy, particularly single-molecule tracking (SMT), have greatly improved our ability to observe DNA glycosylase's one-dimensional diffusion along DNA *in vitro*. A notable study on human 8-oxo-guanine glycosylase (hOGG1) demonstrated its

ability to travel along a 50-kb DNA with an apparent diffusion constant of ~0.58 μm^2/s (ref. [5]). Subsequent reanalysis of single-molecule hOGG1 trajectories using a new optimal estimator of diffusion coefficients uncovered two-state kinetics, wherein the protein switches between a highly mobile (loosely bound) state and a less mobile (tightly bound) state[6]. This finding mirrors ensemble measurements via molecular clock methods, suggesting that the protein adopts a two-state transfer model: associative transfer along the DNA (sliding) and repetitive dissociation and re-binding with the DNA (hopping)[7]. Despite these advances, how DNA glycosylases balance speed and specificity within the heterogeneous nuclear environment remains poorly understood. While SMT experiments of transcription factors in live cells have unraveled multiple diffusional modes[8, 9], DNA glycosylases differ substantially in copy number, target abundance, and functional context. Crucially, conventional SMT lacks spatial resolution, limiting our ability to correlate enzyme dynamics with local nuclear architecture.

To address these challenges, we utilized our recently developed point-cloud single-molecule diffusivity mapping (pc-SM*d*M) technique[10-12] to investigate the diffusivity of hOGG1 in live cell nuclei. Unlike single-molecule tracking (SMT), which tracks individual molecules over time, pc-SM*d*M emphasizes spatial resolution by accumulating the displacements of all molecules traversing a specific area. This approach provides high-resolution, spatially-resolved diffusivity information. Using pc-SM*d*M, we identified four distinct diffusion regions for hOGG1 in native cells, corresponding to key nuclear structures: the nucleolus, nuclear speckles, chromatin territories, and interchromatin compartments. By comparing slow and fast diffusing species within chromatin territories and interchromatin compartments, we estimated the relative contributions of sliding and hopping *in vivo*. Moreover, by combining diffusivity mapping with theoretical simulations, we elucidated the biophysical mechanisms by which the hOGG1 activator TH10785 and the inhibitor TH5487 modulate enzymatic efficiency. We further demonstrated that enzyme performance can be enhanced by modulating the 3D diffusion rate during hopping. These findings highlight the power of spatial mapping in uncovering *in vivo* facilitated diffusion mechanisms and provide deeper insights into the key factors that govern the search efficiency of DNA repair enzymes in their native cellular environment.

Results and Discussions:

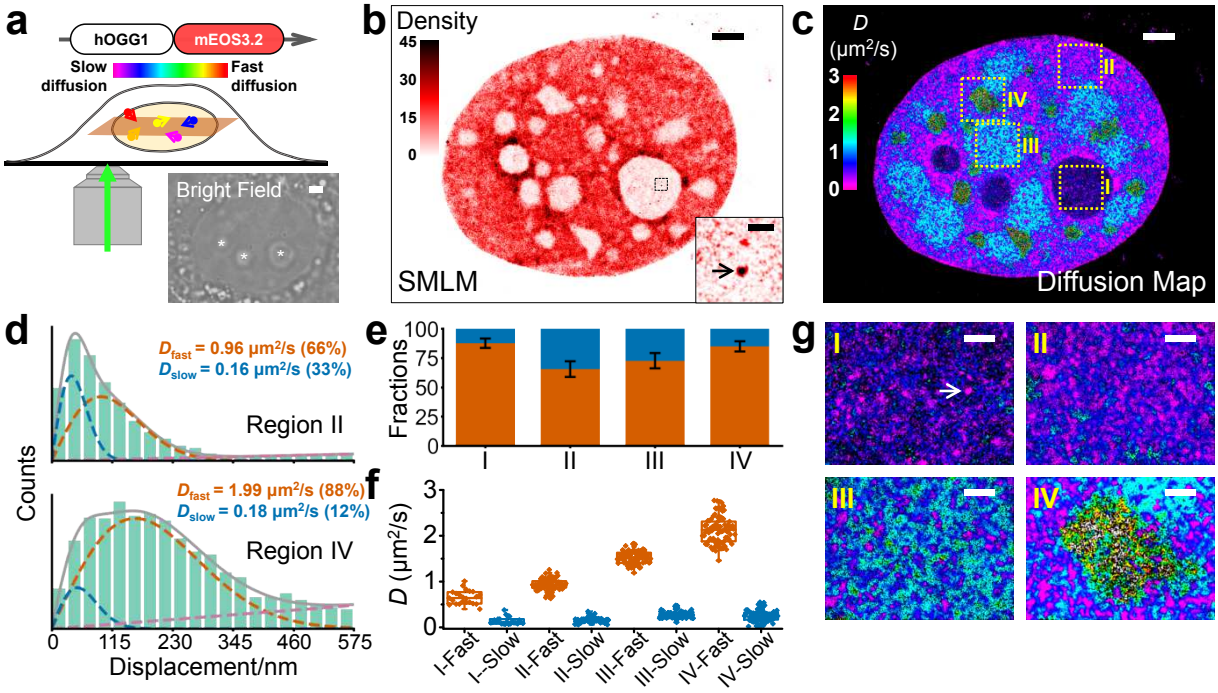

Fig. 1 | hOGG1 displays nanoscale compartmentalization of diffusivity in live cell nuclei.

a). Schematic of mEOS3.2-tagged hOGG1 and imaging setup. Inset: bright-field image of a live cell nucleus.

b). SMLM image showing molecular density of hOGG1. Inset: high-density cluster in nucleolus.

c). pc-SM*d*M diffusion map showing four distinct nuclear regions with varying diffusivity, implying a correlation between local diffusivity and subnuclear architecture.

d). Two-population fitting of Regions II and IV: red, fast species; blue, slow species.

e)-f). Fractions and diffusion rates of fast and slow species across the four regions. Fast species show region-specific *D* values, while slow species remain relatively consistent.

g). Zoomed-in views of the four regions (corresponding to yellow boxes in **c**); white arrow points to slow-diffusing cluster matching inset of panel **b**.

Scale bars: 2 μm (**b**-**c**), 500 nm (**g**), 200 nm (inset of **b**). Color scale consistent across panels. ~60 regions from ~20 cells analyzed (**e**-**f**). Box plots show median (center line), upper and lower quartiles (box limits), and outliers (points).

Compartmentalized diffusion of hOGG1 in nuclei

We initiated the imaging of the DNA repair enzyme by expressing mEOS3.2-tagged hOGG1 in live COS-7 cells. By setting the focal plane a few micrometers into the cell, we were able to image the central plane of the nucleus (Fig. 1a, inset: bright field image). Extended Data Figure

1a shows the epifluorescence image of the nucleus, revealing several regions with minimal fluorescent protein signal. Photoconversion of mEOS3.2 to its red form via a weak 405 nm laser enabled the visualization of single molecules[13], resulting in the single-molecule localization microscopy (SMLM) image in Fig. 1b, where color indicates the local single-molecular density (See Methods).

Next, we performed point-cloud single-molecule diffusivity mapping (pc-SM*d*M) imaging using stroboscopic illumination. By comparing the locations of single molecules between consecutive frames, we obtained millions of displacements from 65,000 frames (Extended Data Fig. 1b). For each single molecule, the nearby displacements were used to construct a histogram from which a single local diffusion rate was extracted (see Methods). The resulting diffusivity map (Fig. 1c) revealed pronounced spatial heterogeneity, with the nucleolus showing the lowest diffusion rates ($D < 0.75$ μm²/s). This region is marked as Region I in Fig. 1c and by the asterisk in the bright field image of Fig. 1a. Depending on the diffusion rates, four distinct regions with different D values were identified (Fig. 1g, corresponding to yellow boxes in Fig. 1c). These heterogeneities suggest that the diffusion of the DNA repair enzyme is strongly influenced by local nuclear structures.

In-depth analysis of the displacement histograms revealed two populations[14]: fast- and slow-diffusing species (red and blue curves in Fig. 1d), consistent across all nuclear regions. The slow-diffusing species are also visible as the magenta clusters in Fig. 1c. We analyzed the fractions and diffusion rates of the two populations within the four regions from 20 cells. For the fast-diffusing species, the diffusion rates are 0.65 ± 0.14, 0.93 ± 0.12, 1.53 ± 0.14, and 2.12 ± 0.28 μm²/s, with fractions of 87.6 ± 3.9%, 65.5 ± 6.8%, 72.6 ± 6.5%, and 84.9 ± 4.3% for regions I, II, III, and IV, respectively (Fig. 1e and 1f). In contrast, the slow-diffusing species have similar rates across all four regions, with values of 0.14 ± 0.07, 0.16 ± 0.05, 0.28 ± 0.07, and 0.25 ± 0.12 μm²/s. Moreover, these magenta clusters with slow diffusion rates often exhibit higher single-molecular density, as indicated by the arrows in region I of Fig. 1g and inset of Fig. 1b (corresponds to black box, Fig. 1b). A strong correlation between the slow-diffusion clusters and high-density regions was also observed in region III, as shown by the images and cross-correlation[15] curve in Extended Data Fig. 1c. Taken together, we suggested that these slow-diffusion clusters, observed across all regions, represent either tight DNA bindings within chromatin regions[16] or interactions with other proteins in chromatin-devoid regions.

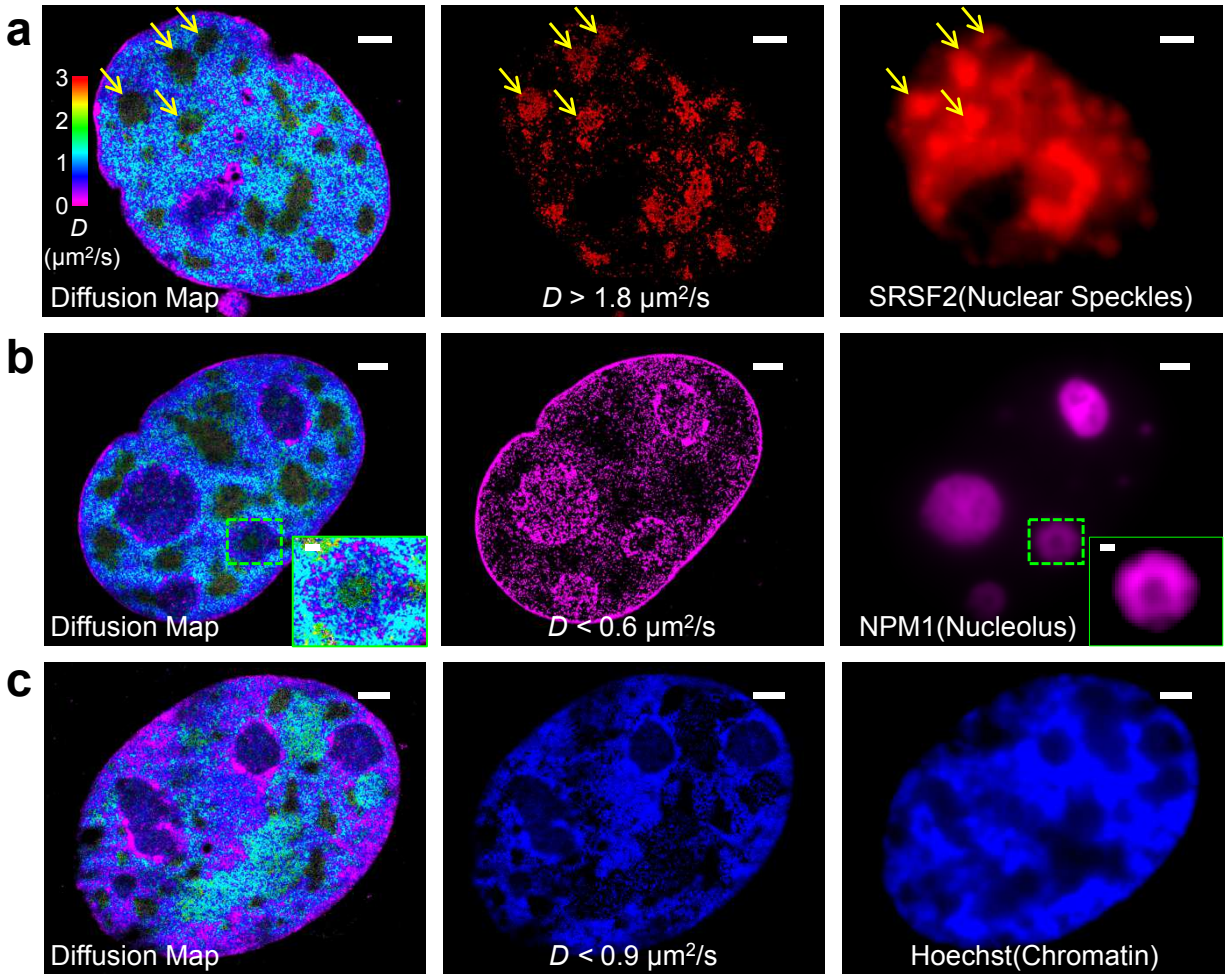

Fig. 2 | Local nuclear architecture defines hOGG1 diffusion heterogeneity.

a). pc-SM*d*M image of hOGG1 (left) and SRSF2 (right) showing fastest diffusion in nuclear speckles (yellow arrows). Middle: SMLM image of fast clusters ($D > 1.8$ μm²/s).

b). pc-SM*d*M image of hOGG1 (left) and NPM1 (right) showing slowest diffusion in nucleoli. Middle: SMLM image of slow clusters ($D < 0.6$ μm²/s). Insets: fast-diffusing intra-nucleolus structure.

c). pc-SM*d*M image of hOGG1 (left) and Hoechst-stained chromatin (right) showing slower diffusion in chromatin territories (CTs) than interchromatin compartments (ICs). Middle: SMLM image highlighting $D < 0.9$ μm²/s in CTs.

Scale bars: 2 μm (**a-c**), 500 nm (inset of **b**). Color scale consistent across panels.

Compartmentalized diffusion reflects nuclear architecture

We next examined the local cellular structures underlying these four regions. Given that hOGG1 is known to be excluded from nuclear speckles—subnuclear structures enriched with pre-mRNA splicing factors and devoid of chromatin[17], we co-expressed iRFP702-tagged SRSF2 with hOGG1-mEOS3.2 and performed diffusivity mapping. Figure 2a (additional images in Extended Data Fig. 2) presents the super-resolution diffusivity map (left panel) alongside the epifluorescence image of SRSF2 (right panel). A clear correlation was observed between the fast-diffusing regions (region IV) and nuclear speckles, as indicated by the yellow arrows. By applying a threshold of D values greater than 1.8 μm²/s, the resulting SMLM image (middle panel) showed a significant overlap with nuclear speckles, underscoring the robustness of our diffusion measurements. Previous studies have reported that positive charges, rather than negative ones, significantly impede the diffusion of non-functional fluorescent proteins[10, 18, 19]. In our study, the net charges of hOGG1 and mEOS3.2-tagged hOGG1 at pH 7.4 are +6.6 and +8.4, respectively (Extended Data Table 1). As nuclear speckles are known to be rich in proteins involved in transcription and RNA processing—many of which, like SRSF2, are positively charged, we propose that the fast diffusion observed within nuclear speckles primarily reflects less electrostatic interactions with negatively charged proteins/RNA in nuclear speckles.

Additionally, we further verified Region I as the nucleolus by co-expressing iRFP702-tagged NPM1 (Nucleophosmin). Figure 2b shows that regions with the slowest diffusion (D < 0.6 μm²/s) correlated well with nucleoli. In some cases, we even observed internal structures insides nucleolus[20] with fast diffusion rates, as highlighted in the zoom-in images in Fig. 2b. These findings again underscore the significance of high spatial resolution in diffusivity mapping for resolving intra-nucleolus ultrastructure.

To confirm the spatial correlation with chromatin, we stained the cell with Hoechst 33342. Figure 2c (additional images in Extended Data Fig. 2) presents the super-resolution diffusivity image (left panel) alongside the epifluorescence image of chromatin (right panel). By applying a threshold for D values below 0.9 μm²/s, the resulting SMLM image (middle panel) revealed significant overlap with chromatin. These images are consistent with the Chromosome Territories and Interchromatin Compartments (CT-IC) model[21]. Interchromatin compartments (ICs) are known to harbor various RNA processing proteins and act as conduits for transport between nuclear pore complexes (NPCs) and chromatin[22]. Chromosome territories (CTs), in contrast, serve as the primary working sites for hOGG1, where it slides along chromatin to recognize its binding partner—8-oxo-Guanine—resulting in slower diffusion (Region II) compared to the ICs (Region

III). As a result, the observed differences in diffusion rates between CTs and ICs are primarily attributed to the bindings of hOGG1 with chromatin in CTs.

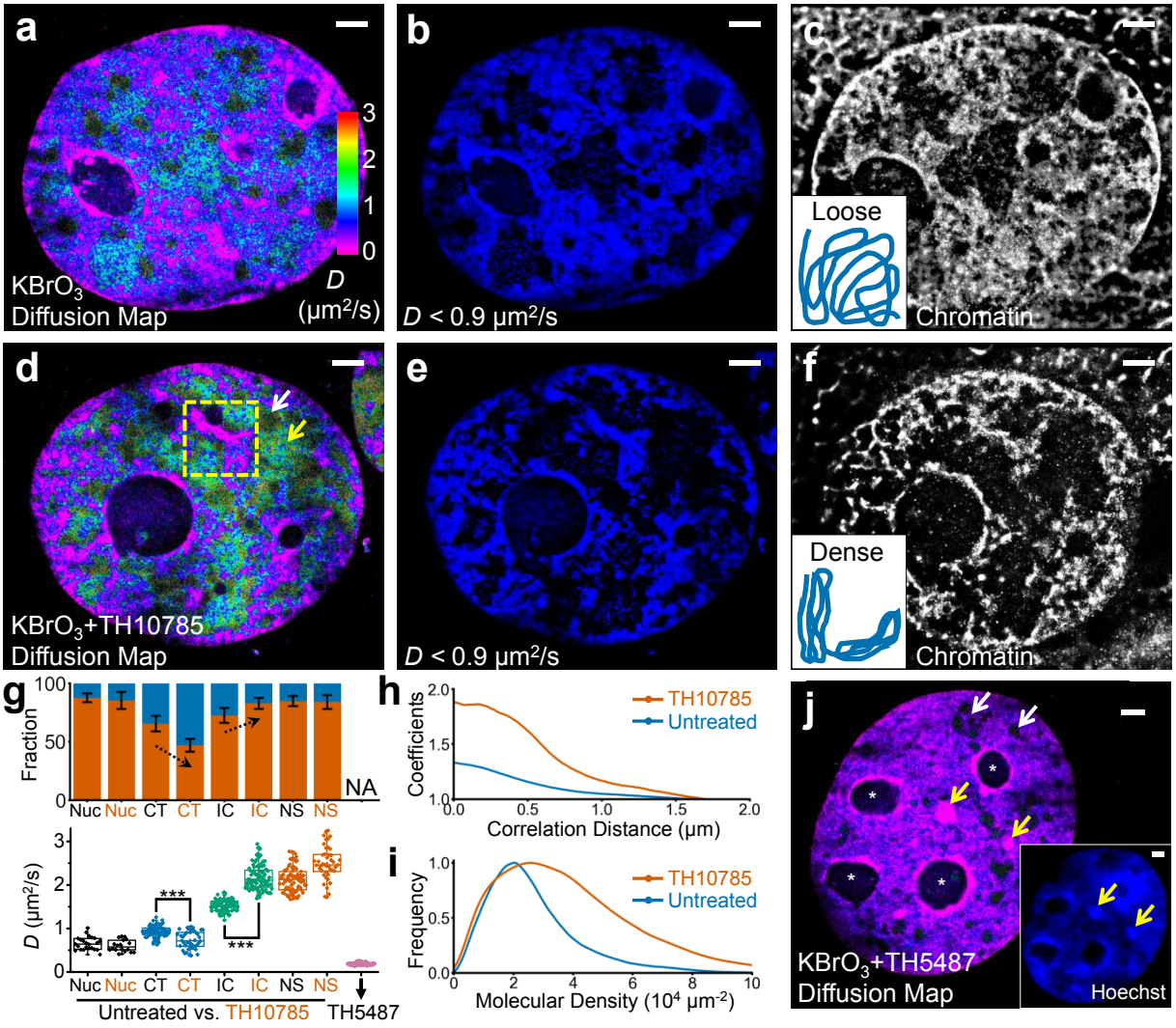

Fig. 3 | Activator enhances hOGG1 repair by modulating diffusion and chromatin compaction.

a). pc-SM*d*M image after oxidative stress shows no major change in diffusivity.

b). SMLM image highlighting regions with $D < 0.9$ μm²/s, corresponding to chromatin territories in panel **a**.

c). SMLM image of chromatin with DNA stains corresponding to panel **a**, showing loosely packed chromatin.

d)-f). pc-SM*d*M and SMLM images after oxidative stress and subsequent activation with TH10785. CTs become compact (yellow box), with reduced diffusivity; ICs expand and show increased diffusivity (yellow arrow), approaching those seen in nuclear speckles (white arrow).
g). Quantification of diffusion rates and population fractions of fast- (red) and slow-diffusing (blue) species across four nuclear regions before and after activation.
h). Cross-correlation between slow-diffusing clusters and chromatin increases upon activation.
i). Chromatin density histograms from **c** and **f** show compaction upon activation.
j). pc-SM*d*M image after inhibitor (TH5487) shows global slowdown and chromatin-associated clusters. Inset: Hoechst staining.
Scale bars: 2 μm. Color scale consistent across panels. ~60 regions from ~20 cells analyzed (**g**). Box plots show median (center line), upper and lower quartiles (box limits), and outliers (points).

Activator-induced chromatin compaction boosts enzyme efficiency

To investigate how diffusional states reflect different repair efficiencies, we examined the effects of both an activator and an inhibitor on hOGG1's diffusion behavior. Recent studies have shown that the small molecule TH10785 functions as an activator by inducing a novel lyase activity and boosting enzymatic performance tenfold[23], although how it affect the enzyme's search efficiency remains unclear. To investigate this, we treated cells with 20 mM $KBrO_3$ for one hour to induce oxidative damage, followed by 10 μM TH10785 treatment for 6 hours (see Methods). Oxidative stress alone did not significantly alter hOGG1 diffusivity (Fig. 3a). In contrast, TH10785 treatment induced marked changes in CTs and ICs (Fig. 3d). The ICs (yellow arrow, Fig. 3d) expanded, occupying more nuclear space, with increased diffusion rates approaching those seen in nuclear speckles (white arrow, Fig. 3d). In contrast, the CTs became more condensed, transforming into condensates with significantly reduced diffusion rates (magenta condensates in the yellow box, Fig. 3d). Statistical analysis of diffusion rates and population fractions in chromatin territories (CTs) and interchromatin compartments (ICs) is shown in Fig. 3g, along with data from untreated cells. Upon activation, hOGG1 exhibited decreased diffusion rates (0.73±0.20 $\mu m^2/s$) in CTs and increased diffusion rates (2.17±0.29 $\mu m^2/s$) in ICs. The fraction of slow-diffusing species increased in CTs (53.0±5.4%) but decreased in ICs (17.2±4.7%), suggesting enhanced chromatin compaction and increased binding events in CTs upon activation.

These architectural changes prompted further examination of chromatin structure via SMLM. After diffusivity mapping, cells were fixed and subjected to SMLM imaging of chromatin/DNA

using NucSpot 650 (ref. [10]). Figs. 3b, 3c, 3e, and 3f show correlative images of SMLM maps (D < 0.9 μm²/s) and chromatin structure under two treatment conditions. In the absence of the activator, chromatin appeared loosely packed and occupied a larger nuclear volume, yielding clear cross-correlations between slow-diffusing regions and high-density chromatin (blue curve in Fig. 3h). Following activator treatment, chromatin became more densely packed, resulting in an even stronger cross-correlation between slow-diffusing regions and high-density chromatin areas (red curve in Fig. 3h). Additionally, molecular density analysis revealed a marked increase in chromatin upon activation (Fig. 3i), further supporting the conclusion that TH10785 induces chromatin compaction.

The observation that activation promotes hOGG1 condensates at compact chromatin sites is consistent with previous findings that activation of hOGG1's lyase function leads to its recruitment to damaged chromatin and the formation of DNA repair foci[23]. We hypothesize that this clustering may also indicate the assembly of heterochromatin. Indeed, co-expression of iRFP702-tagged HP1α revealed clear colocalization between hOGG1 condensates and heterochromatin (Extended Data Fig. 3). Diffusivity mapping further demonstrated that slow-diffusing hOGG1 clusters closely correspond to heterochromatic regions (arrows in Extended Data Figs. 3a and 3b). Overlaying the pc-SM*d*M images with the HP1α epifluorescence image revealed that these clusters often surround HP1α (Extended Data Fig. 3c), suggesting that hOGG1 forms condensates both within and around heterochromatin. Heterochromatin is known to be more vulnerable to DNA damage, as its compact structure limits the access of repair enzymes[24, 25]. For DNA double-strand breaks, studies have shown that such breaks in heterochromatin are often sequestered to its periphery to facilitate repair[26, 27]. Using spatially resolved diffusivity mapping, we also found that the activator TH10785 strengthens hOGG1's interactions with chromatin, promoting the formation of condensates in and around heterochromatin with slower diffusion rates.

As a comparison, we also investigated the diffusional behavior of hOGG1 following treatment with the inhibitor TH5487, which is known to impair hOGG1's enzymatic activity[28]. The resulting pc-SM*d*M image (Fig. 3j) revealed widespread formation of clusters throughout the nucleus, characterized by extremely slow diffusion rates (D = 0.19±0.03 μm²/s, Figs. 3g and 3j). These clusters were less prevalent in certain regions, presumably nucleoli and nuclear speckles (asterisk and white arrows in Fig. 3j). Correlative imaging with Hoechst staining showed that these slow-diffusing species colocalized clearly with chromatin (yellow arrows in Fig. 3j), suggesting that the inhibitor induces tight binding of hOGG1 to chromatin while abolishing its catalytic function.

Together, our pc-SM*d*M images demonstrate that the diffusion behavior of hOGG1—and its spatial association with chromatin—faithfully reflects its functional states during both enzymatic activation and inhibition.

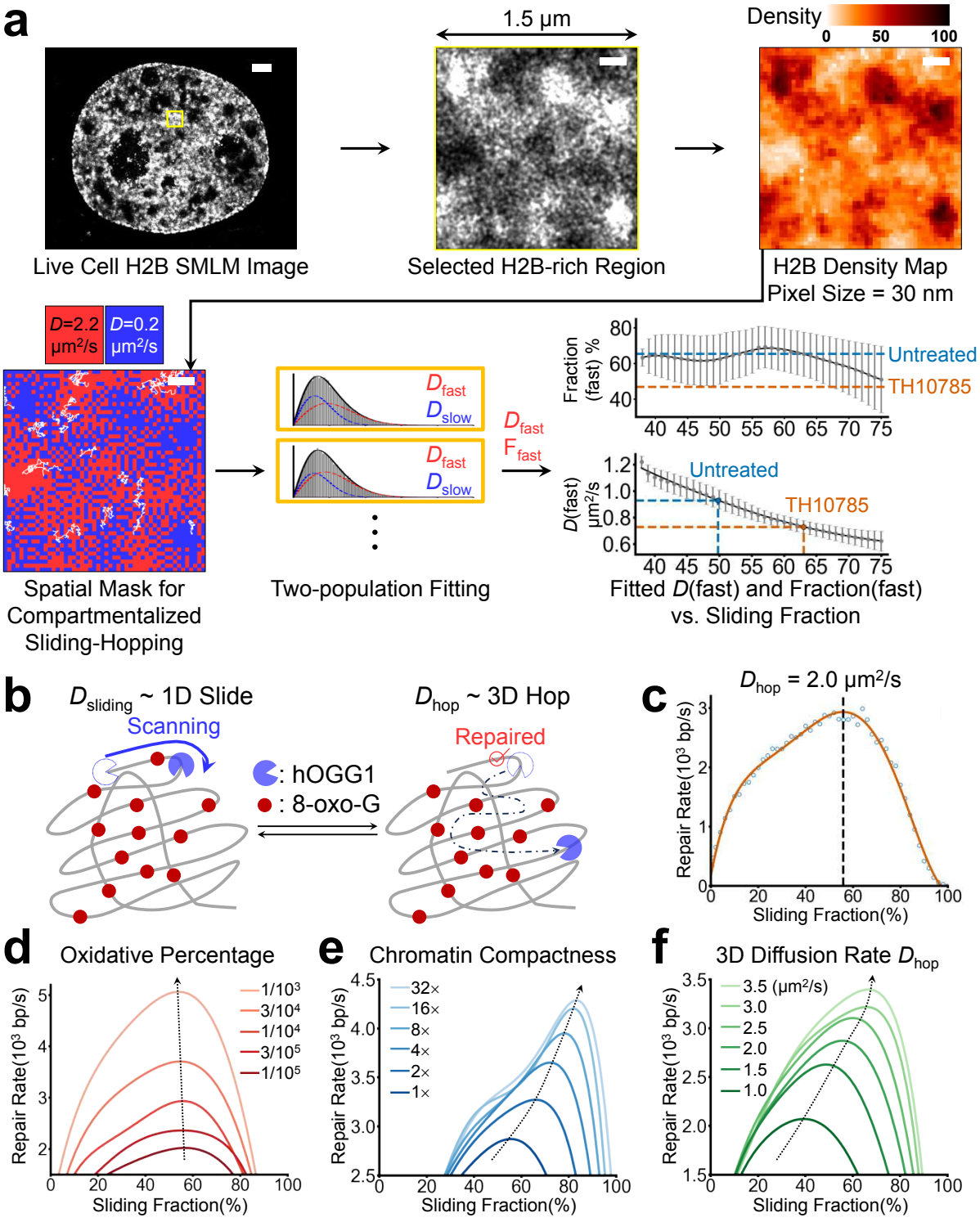

Fig. 4 | Simulations reveal determinants of optimal hOGG1 search efficiency.

a). Simulation mask generated from H2B SMLM images based on the compartmentalized sliding-hopping (CSH) model, Red and blue denote hopping and sliding units. Millions of trajectories simulated. Two-population fitting yields D_{fast} and F_{fast} as functions of the sliding fraction, allowing direct comparison with experimental data to determine the sliding fraction *in vivo* (see main text).

b). Schematic of the facilitated diffusion model: 1D sliding scans DNA; 3D hopping bypasses segments. Only oxidized guanines encountered during sliding were considered repairable.

c). Repair rate as a function of sliding fraction shows the optimal fraction at ~55%.

d). Increasing oxidative lesion density had little effect on the optimal sliding fraction.

e). Higher chromatin compaction improves repair rate but shifts optimal sliding fraction upward.

f). Faster 3D hopping enhances repair and increases optimal sliding fraction.

Scale bars: 2 μm (SMLM image of **a**), 200 nm (**a**). Note: y-axes in **d-f** truncated for clarity. ~50 masks from ~20 cells with 10^7 trajectories per mask simulated. Error bars represent standard deviations.

Mechanistic insights into enzymatic search efficiency

To further understand how hOGG1's diffusional behavior is modulated by enzyme activation, we employed Monte Carlo simulations based on the facilitated diffusion model, which integrates one-dimensional sliding along DNA with intermittent three-dimensional hopping[4, 29]. Sliding enables local scanning by maintaining DNA contact, but is inefficient for locating rare targets across the genome. In contrast, hopping allows the enzyme to transiently dissociate and rebind at distant sites, increasing search range but skipping base pairs in between. An optimal balance between sliding and hopping is thus required for efficient lesion search.

To capture spatially resolved sliding versus hopping dynamics within chromatin territories (CTs), we performed live-cell SMLM imaging of mEOS3.2-tagged H2B (Fig. 4a). The resulting H2B distribution, along with the hOGG1 diffusivity map in CTs (Fig. 1g), revealed intrinsic heterogeneity in chromatin organization—suggesting that hOGG1 may even experience spatial heterogeneity in terms of sliding-to-hopping ratios within CTs. To simplify this spatial complexity, we generated 30 nm-resolution density maps and introduced a compartmentalized sliding-hopping (CSH) model. In this framework, each 30 × 30 nm² unit—matching the scale of 30-nm chromatin fibers[30] —was assigned either sliding or hopping behavior based on local H2B

density. In the resulting spatial mask, red and blue denote hopping (D_{hop} = 2.2 μm^2/s) and sliding ($D_{sliding}$ = 0.2 μm^2/s) units, respectively, enabling large-scale simulation of hOGG1 trajectories (See Methods for details). ~50 spatial masks from ~20 cells were generated, and two-population fitting of the simulated displacement distributions yielded (D_{fast}) and its fraction (F_{fast}), which were plotted as a function of sliding fraction (defined as the fraction of sliding units on the spatial mask). Based on the experimentally measured D_{fast}, we estimate that ~50% of hOGG1 search activity in CTs involves sliding under basal conditions, increasing to ~63% following TH10785 activation (bottom right panel in Fig. 4a; see Methods).

To further test whether the estimated sliding fraction aligns with the optimal search strategy, we simulated hOGG1's search along a single chromatin fiber, where only oxidized guanines encountered during 1D sliding were considered repairable (Fig. 4b; see Methods). The repair rate—defined as the number of lesions per second—peaked at ~55% sliding fraction (Fig. 4c), aligning with the CSH model and prior prediction[31]. Increasing lesion density from 1 in 10^5 to 1 in 10^3 base pairs had little effect on the optimal sliding fraction (Fig. 4d), suggesting that hOGG1 maintains efficient search behavior across varying levels of oxidative stress. Mimicking chromatin condensation by increasing DNA packing density from 1.6×10^6 to 5.12×10^7 bps/μm^3 (ref. [32]) elevated the repair rate but required a higher sliding fraction for optimal efficiency (Fig. 4e), consistent with increased sliding fraction following TH10785 activation. Finally, raising the 3D diffusion rate during hopping (1.0–3.5 μm^2/s) further boosted repair efficiency and shifted the optimal sliding fraction upward (Fig. 4f). Since positively charged proteins face electrostatic hindrance in the nucleus[10], reducing net charge could enhance 3D diffusion[18, 19] and improve repair performance—offering a biophysically grounded strategy for enzyme optimization.

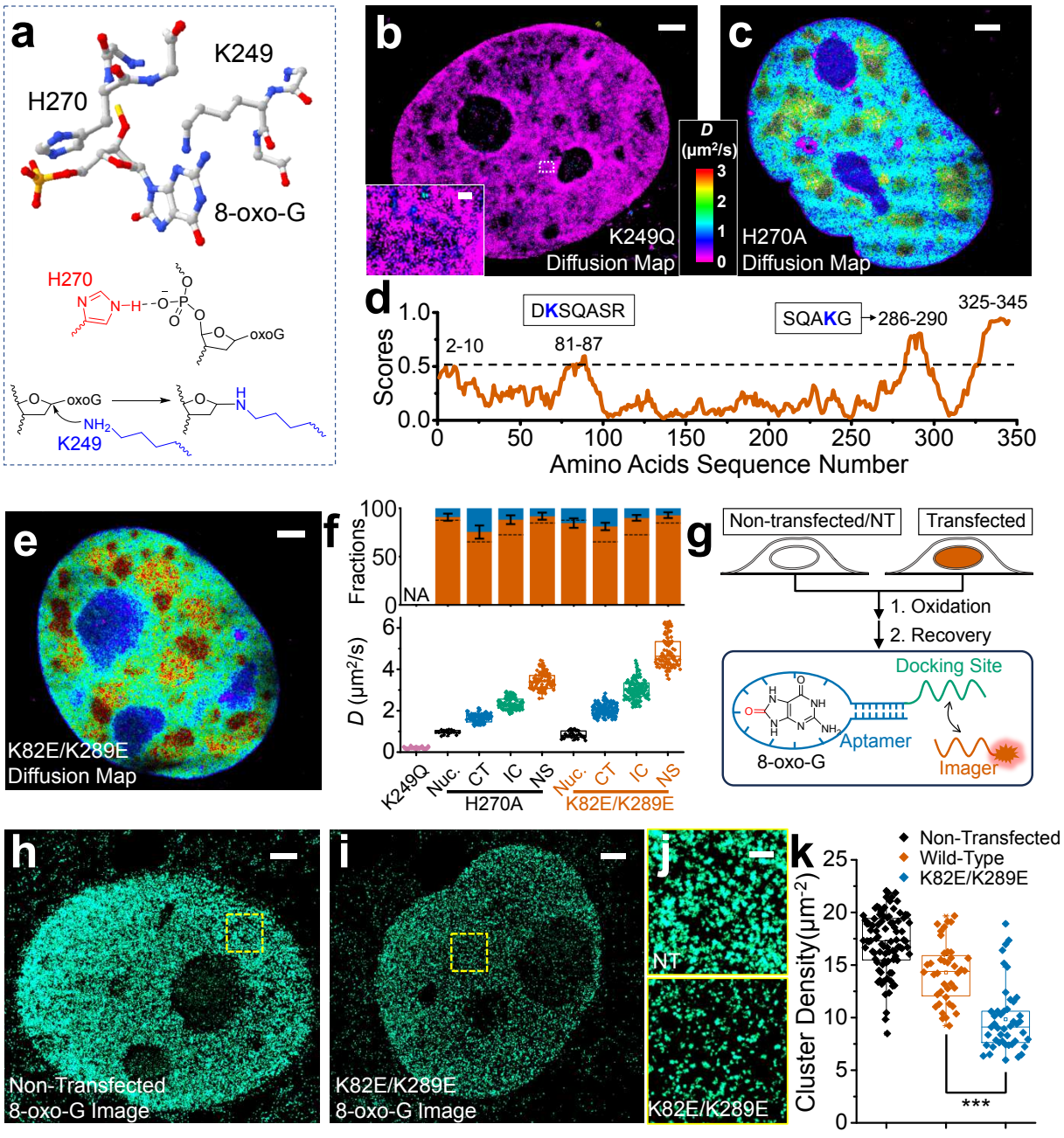

Fig. 5 | Charge-reducing mutations enhance hOGG1 diffusivity and repair efficiency.

a). Structure of hOGG1 with residues K249 and H270 involved in lesion recognition and catalysis (PDB ID: 1EBM).

b). K249Q mutant displayed reduced diffusion in the nucleus, indicating long-lived chromatin binding. Inset: zoomed-in image of the white box highlights the slow-diffusing species.

c). H270A mutant exhibited increased nuclear diffusion, suggesting weakened chromatin interactions.

d). Predicted disordered regions (residues 81–87, 286–290) via IUPred2 targeted for mutation.

e). K82E/K289E mutant showed markedly increased diffusivity.

f). Diffusion rates and species fractions for various mutants. Dashed lines show wild-type benchmarks.

g). Schematic of DNA-PAINT imaging of 8-oxo-G via aptamer binding in fixed cells for non-transfected (NT) and transfected cells.

h)-i). DNA-PAINT imaging of 8-oxo-G lesions shows reduced lesion density in cells expressing K82E/K289E compared to non-transfected (NT) controls.

j). Zoomed-in images of the yellow boxes in panels **h** and **i**.

k). Comparison of cluster densities in non-transfected cells, cells overexpressing wild-type hOGG1, and cells overexpressing K82E/K289E. The density in K82E/K289E-transfected cells was even lower than in wild-type hOGG1-transfected cells, suggesting improved enzymatic performance.

Scale bars: 2 μm (**b, c, e, h,i**), 500 nm (**j**), 200 nm (inset of **b**). Color scale consistent across panels. ~60 regions from ~20 cells analyzed in **f** and **k**. Box plots show median (center line), upper and lower quartiles (box limits), and outliers (points).

Enzymatic efficiency tuned by net charge modulation

Given that hOGG1 carries a net positive charge (+6.6 at pH = 7.4), we next examined the diffusion behavior of various hOGG1 mutants. We began by studying two well-characterized mutants with opposing effects on their interaction with oxidative G: K249Q and H270A. Figure 5a presents the DNA-protein interface[33] (PDB ID: 1EBM), highlighting key residues K249 and H270. Lys 249 acts as a nucleophilic residue essential for excising the damaged base[33] (Fig. 5a). The K249Q mutation, which removes its catalytic activity while retaining substrate recognition[34], led to a significant diffusion slowdown and accumulation at chromatin territories (CTs), as shown in Fig. 5b. These slow-diffusing species (Zoom-in, Fig. 5b) reflect long-lived binding to oxidative G without subsequent cleavage. In contrast, His 270 forms a hydrogen bond with the 5' phosphate of the oxidative G nucleobase, contributing to base recognition and discrimination during repair[33, 35] (Fig. 5a). The H270A mutation, which reduces binding affinity with oxidative G by over 30-fold[36], resulted in a global increase in diffusion (Fig. 5c).

To increase 3D diffusion without impairing function, we targeted positively charged residues in disordered regions not involved in substrate binding (Fig. 5d). By substituting the positively charged lysines K82 and K289 with negatively charged glutamates (E), we generated a mutant

hOGG1 variant with increased diffusion rate (Fig. 5e). This charge reduction, from +6.6 to +2.6, led to approximately a twofold enhancement in diffusion (Fig. 5f). These findings align with our earlier observations, reinforcing the notion that proteins with reduced positive charge exhibit faster diffusion in the nucleus[10, 18].

To evaluate the repair efficiency of the K82E/K289E variant, cells were fixed following transfection, 1-hour oxidation, and a 6-hour recovery period. Subsequently, 8-oxo-G lesions were labeled using an aptamer[37, 38] conjugated with a docking DNA strand (Fig. 5g), allowing reversible binding of a fluorescently labeled imager strand with a complementary sequence. This facilitated super-resolution imaging of 8-oxo-G via DNA-PAINT[39-41]. Comparisons between non-transfected (NT) and transfected cells within the same sample (Figs. 5h and 5i) revealed significantly fewer 8-oxo-G clusters in transfected cells, an observation further highlighted in the zoomed-in images (Fig. 5j). Quantification using density-based clustering (DBSCAN) demonstrated reduced cluster densities upon overexpression of both the wild-type and K82E/K289E variants of hOGG1 (Extended Data Fig. 4). Notably, the K82E/K289E variant exhibited an even lower cluster density than the wild type, suggesting enhanced repair efficiency (Fig. 5k and Extended Data Fig. 4). Consistent with our simulations, this improvement was attributed to the higher search efficiency of the K82E/K289E variant (Fig. 4f). Control experiments without the aptamer-docking strand showed significantly fewer 8-oxo-G clusters in the nuclei (Extended Data Fig. 5). These results establish that increasing the diffusion rate during hopping can significantly enhance the repair efficiency of hOGG1 in live cells.

Discussions:

Prior approaches lacked the spatial resolution to link diffusion states with nuclear architecture. Using pc-SM*d*M, we mapped hOGG1 dynamics in live nuclei and identified distinct diffusion behaviors associated with specific subnuclear compartments. Diffusion was fastest in nuclear speckles and slowest in the nucleolus, with intermediate rates observed in chromatin territories (CTs) and interchromatin compartments (ICs). Interestingly, although diffusion in CTs was slower than in ICs, the concentration of hOGG1 remained uniform across both regions (Fig. 1b and Extended Data Fig. 1a), suggesting similar levels of macromolecular crowding. This aligns with our previous findings that negatively charged proteins experience minimal crowding effects in CTs when compared to ICs[10]. These results indicate that the diffusion slowdown in CTs compared to ICs is primarily due to interactions with chromatin, rather than crowding effects. Given that

hOGG1 is capable of sliding along DNA, we interpret this as evidence of active sliding rather than static binding. Quantitative simulation estimated that sliding accounts for ~50% of the overall search dynamics within CTs. These findings underscore the importance of spatial resolution in probing the behavior of DNA repair enzymes in live cells and provide mechanistic insight into the multiple diffusion species observed for other DNA-interacting proteins and transcription factors in single-molecule tracking studies[8, 42-44]. Long-lived binding species[16, 45] appeared immobilized in our experiments, with diffusion coefficients below 0.1 $\mu m^2/s$—beyond the lower limit of our measurements with ~6 ms tracking time. However, their fraction was very low (<1%) in our experiments and thus has limited impact on our model.

Leveraging the advantages of spatial resolution, we elucidated the extra new mechanism by which the recently discovered hOGG1 activator[23] TH10785 enhances enzymatic activity through improved search efficiency. Using correlative super-resolution imaging of DNA/chromatin and two-color imaging with HP1α, we found that TH10785 modulates hOGG1 diffusivity by inducing chromatin compaction and promoting the formation of hOGG1 condensates in heterochromatin regions. Notably, our analysis revealed increased sliding motion in heterochromatin upon activation, with quantitative simulations indicating that sliding contributes ~63% to the overall search dynamics. These changes collectively enhance enzymatic repair efficiency, a conclusion further supported by theoretical simulations. This finding bridges the gap between chromatin compaction, enzymatic activity, and molecular diffusion, offering new insight into how intranuclear structural reorganization can elevate the efficiency of DNA repair.

The diffusion rate is a critical factor influencing chemical reaction rates, as faster diffusion increases the collision frequency of reactants. Building on our previous findings that proteins diffuse faster with reduced positive charge in live cell nuclei, and informed by theoretical simulations in this study, we hypothesized that mutating positively charged amino acids in the disordered regions—those not directly involved in substrate recognition or catalytic activity—could enhance search efficiency without compromising enzymatic function. By direct imaging of 8-oxo-G in cells transfected with various hOGG1 variants, we identified K82E/K289E as a key mutant with faster diffusion rates and higher repair efficiency, supported by the reduced presence of 8-oxo-G lesions in the nucleus.

It is important to note that the disordered regions of hOGG1 may have additional functions, such as facilitating biomolecular condensate formation[46-48]. This complexity is exemplified by variants with mutations in certain positively charged residues, which failed to exhibit faster

diffusion rates (Extended Data Fig. 6). These results suggest potential screening effects of their charges by hOGG1's binding partners or post-translational modification. Consequently, the strategy of mutating positively charged amino acids in disordered regions cannot be universally applied; each site must be carefully assessed to determine its impact on diffusion and repair efficiency. Evaluating enzymatic efficiency of these mutants *in vitro* presents challenges, as the heterogeneous nuclear environment plays a crucial role in modulating the diffusion behavior of charged proteins. A promising alternative is to quantify enzymatic activity in nuclear extracts, which more accurately replicate the intranuclear environment[49].

Conclusions:

This study demonstrates how spatially resolved single-molecule diffusivity mapping can reveal the interplay between nuclear architecture and enzymatic dynamics in live cells. By tracking hOGG1 in its native environment, we identify three key determinants of its search efficiency: chromatin compactness, the balance between one-dimensional sliding and three-dimensional hopping, and the diffusion rate during hopping. Chromatin condensation, induced by a small-molecule activator, enhances repair efficiency by promoting sliding, while reduced net positive charge accelerates hopping and further boosts enzymatic performance. These findings establish a direct link between local chromatin organization, electrostatic properties, and enzymatic function. More broadly, they suggest a generalizable strategy for modulating intracellular enzyme activity through physicochemical tuning—providing conceptual and practical avenues for improving DNA repair and cellular homeostasis.

Methods

Chemicals and components of buffers: Hoechst 33342: Purchased from Shanghai Macklin Biochemical Co., Ltd., used for nuclear staining. NucSpot® Live 650: Purchased from Biotium (Cat. No. 40082), a live-cell nuclear dye. $KBrO_3$ was purchased from Macklin Biochemical Co., Ltd. TH10785 (Activator): Obtained from TargetMol, used as an activator. TH5487 (Inhibitor): Procured from Shanghai Yuanye Bio-Technology Co., Ltd., used as an inhibitor. Live Cell Imaging Buffer: Leibovitz's L-15 medium (Gibco 21083027) supplemented with 20 mM HEPES buffer (Gibco 15630106) for optimal pH stabilization during live-cell imaging. Fixed Cell STORM Imaging Buffer: Prepared with 100 mM Tris–HCl (pH 8.0), 20 mM NaCl, 100 mM

cysteamine, and 10% glucose. An oxygen-scavenging system comprising 60 mg/mL glucose oxidase and 6 mg/mL catalase (both from Sigma-Aldrich) was added to minimize photobleaching during fixed-cell STORM imaging experiments. Blocking Buffer (BB) in immunolabeling: Consisting of 3% BSA and 0.5% Triton X-100 in PBS. Stored at 4 °C. Washing Buffer (WB) in immunolabeling: Composed of 0.2% BSA and 0.1% Triton X-100 in PBS. Stored at 4 °C. Aptamer Binding Buffer: 5 mM $MgCl_2$, 0.1 mg/ml Salmon dsDNA (Thermofisher), 1 mg/ml dextran sulphate sodium, 0.1 mg/ml RNase A (Thermofisher), and 0.5% Triton-X in 1×PBS. Aptamer Imaging Buffer: 5 mM $MgCl_2$, 0.1 mg/ml Salmon dsDNA (Thermofisher), and 0.1 mg/ml dextran sulphate sodium in 1×PBS.

Plasmid construction: The mEos3.2-C1 plasmid (Addgene #54550), a gift from Michael Davidson and Tao Xu, was used as a backbone to construct hOGG1-mEos3.2 by fusing the hOGG1 sequence (Addgene #18709, provided by David Sidransky) to the N-terminus of mEos3.2 at the AgeI restriction site. The piRFP702-N1 plasmid (Addgene #45456), a gift from Vladislav Verkhusha, served as a backbone for creating iRFP702-tagged SRSF2, NPMI, and HP1α constructs by inserting their respective DNA sequences (purchased from Miaolingbio Inc., plasmids #P3758 for SRSF2, #P61047 for NPMI, and #P35426 for HP1α) into the C-terminal region of iRFP702 between SacI and BamHI restriction sites. mEOS3.2-H2B was constructed by inserting their respective DNA sequences (purchased from Miaolingbio Inc., plasmids #P44472 for H2B) into the C-terminal region of mEOS3.2-C1 between SacI and SalI restriction sites. Mutations K249Q, H270A, and K82E/K289E within the hOGG1 coding sequence were introduced using the Phusion Site-Directed Mutagenesis Kit (ThermoFisher Scientific) based on the full-length mEos3.2-tagged hOGG1. Detailed information on all plasmids is summarized in Extended Data Table 1, and all sequences were verified through Sanger sequencing.

Coverslips preparations: Glass coverslips (18 mm in diameter) were first treated with piranha solution (a 3:1 mixture of sulfuric acid and hydrogen peroxide) heated for 15–20 minutes. The solution was allowed to cool, and the coverslips were thoroughly rinsed with Milli-Q water (18.4 MΩ·cm) and dried with nitrogen gas. The cleaned coverslips were then placed in a 12-well plate and sterilized under UV light for 15 minutes in a biosafety cabinet.

Cell Culturing and Transfection: COS-7 cells (Wuhan Pricella Biotechnology Co., Ltd, CL-0069) were cultured in Dulbecco's Modified Eagle's Medium (DMEM) supplemented with 10% fetal bovine serum (FBS) and 1% penicillin-streptomycin in a humidified incubator at 37°C with 5% CO_2. Approximately 48–72 hours before imaging, cells were electroporated using a Bio-Rad

electroporation system (100 V, 20 ms, 0.2 cm cuvette) in electroporation buffer containing ~10^5 cells and 5 μg plasmid DNA per sample. The cell suspension was then plated onto the prepared coverslips with 1 mL of freshly warmed culture medium and mixed gently to ensure even distribution. Prior to imaging, the samples were rinsed three times with prewarmed imaging buffer to remove residual culture medium. The coverslips were mounted onto a sample holder (Bioscience Tools, CSC-18), and 1 mL of imaging buffer was added to the imaging chamber for pc-SM*d*M experiments. For co-expression studies, two plasmids were simultaneously transfected using the same protocol as described above.

Oxidative stress and drug treatment: To induce oxidative DNA damage, cells at approximately 80% confluency were treated with 20 mM $KBrO_3$ in serum-free DMEM for one hour. Following this, the cells were incubated with 1 mL of fresh medium containing either 10 μM TH10785 (activator), 10 μM TH5487 (inhibitor), or an equivalent volume of DMSO for six hours. After treatment, the cells were washed three times with PBS to remove residual compounds and then mounted onto the sample holder with imaging buffer for imaging.

Optical setup: SMLM and pc-SM*d*M experiments were conducted on a custom-built system based on an Olympus IX83 inverted fluorescence microscope. The system utilized lasers with wavelengths of 405 nm (CNIlaser, MDL-III-405, 500 mW), 488 nm (OBIS 488 LX, Coherent, 150 mW), 532 nm (CNIlaser, OEM-U-532, 500 mW), 560 nm (MPB Communications, 500 mW), and 642 nm (MPB Communications, 500 mW). These lasers were focused at the back focal plane of an oil-immersion objective lens (Olympus UPLXAPO 100x, NA 1.45) to illuminate the coverslip–sample interface slightly below the critical angle, penetrating a few micrometers into the cell. The power output of the 561 nm and 642 nm lasers was precisely regulated via an acousto-optic tunable filter (AOTF, Gooch & Housego). A multifunction input/output (I/O) board (PCIe-6323, National Instruments) was employed to synchronize the AOTF with the exposure output TTL (transistor-transistor logic) signal from the sCMOS camera (Teledyne Photometrics, Prime 95b) and laser operation, achieving an effective exposure time of 2 ms.

SMLM and pc-SM*d*M of live cells: Single-molecule images of mEOS3.2-tagged hOGG1 or mEOS3.2-tagged H2B were continuously recorded over a wide field of ~250×250 pixels for up to 65,000 frames. Imaging was conducted under 561 nm laser excitation at a power density of ~0.2 kW/cm² and photo-activation with a 405 nm laser at a power density of ~2 W/cm². Fluorescence signals were filtered using a longpass filter (ET575lp, Chroma) and a bandpass

filter (ET605/70m, Chroma). Data acquisition was achieved using an sCMOS camera (Teledyne Photometrics, Prime 95b) with a frame rate of ~145 Hz and an effective exposure time of 2 ms. For co-expression experiments, the epifluorescence images of piRFP702-N1-tagged SRSF2, NPMI, and HP1α were first acquired under excitation with a 642 nm laser at a power density of ~6 W/cm². Fluorescence signals were filtered using a longpass filter (ET655lp, Chroma) and a bandpass filter (ET705/100m, Chroma). Images were captured at a frame rate of ~10 Hz and an effective exposure time of 100 ms. To minimize crosstalk, the iRFP702 signal was photobleached using a higher power laser before recording pc-SMdM images of mEOS3.2-tagged hOGG1.

For live-cell imaging of chromatin/DNA, Hoechst 33342 was added to the imaging buffer at a final concentration of 5 μg/mL and incubated at room temperature for 15 minutes. Following pc-SMdM imaging of mEOS3.2-tagged hOGG1, the epifluorescence image of Hoechst 33342 was recorded under excitation with a 405 nm laser at a power density of ~6 W/cm². Fluorescence signals were filtered using a bandpass filter (ET445/58m, Chroma). Images were collected at a frame rate of ~10 Hz with an effective exposure time of 100 ms.

SMLM imaging of fixed cells: After live-cell imaging, the sample was chemically fixed directly on the microscope stage for subsequent fluorescence labeling and SMLM imaging. To investigate the colocalization of chromatin with hOGG1, transfected cells were fixed with 4% paraformaldehyde in PBS and washed three times with PBS. Chromatin was then labeled using NucSpot Live 650 (diluted 1:1000 in PBS) and incubated for 20 minutes. After labeling, the sample was washed twice with PBS and incubated in 1 mL of STORM imaging buffer. SMLM was performed on the same microscope setup under 642 nm laser excitation at a power density of ~0.2 kW/cm², with a frame rate of ~145 Hz and an effective exposure time of 2 ms. Fluorescence signals were filtered using a longpass filter (ET655lp, Chroma) and a bandpass filter (ET705/100m, Chroma).

DNA-PAINT imaging of 8-oxo-G in fixed cells: Cells were transfected with wild-type hOGG1 or its variants, followed by cultured for 24–48 hours. Oxidation treatments and recovery protocols were performed as described above. Afterward, cells were fixed using 4% paraformaldehyde in PBS and washed three times with PBS. Fixed cells were incubated for 1 hour in aptamer binding buffer containing 100 nM aptamer, followed by two rinses with aptamer imaging buffer. Subsequently, 0.2 nM imager strand was introduced for DNA-PAINT imaging. To differentiate transfected and non-transfected cells, epifluorescence images of mEOS3.2 were

collected prior to DNA-PAINT imaging. DNA-PAINT imaging was conducted using a microscope equipped with a 642 nm laser, operating at a power density of ~0.1 kW/cm². Images were acquired at a frame rate of ~125 Hz with an effective exposure time of 2 ms per frame. Fluorescence signals were filtered using a longpass filter (ET655lp, Chroma) and a bandpass filter (ET705/100m, Chroma). The following DNA sequences were used:

Aptamer sequences with docking strand (aptamer-docking strand). The aptamer is underlined while docking strand is italic:

5′- *TCTCTCTCTCTCTCTCTCTCTCTCTCTCTCTCTCTCTCTCTCTCTCTCTCTCTCTC TCTC*TTTTTTTTTTTCGGGACGACGGGCCAGTAACTAGCTCACTCATTACACTTGGTC GTCCC-3′

Imager strand: 5′-GAGAGAGA-3′-AF647

Data analysis for pc-SM*d*M: Single-molecule images were analyzed by fitting each localization of single molecules with a 2D Gaussian function to determine the centroid positions of individual molecules. These positions were then accumulated to reconstruct the single-molecule localization microscopy (SMLM) image. SM*d*M analysis was performed as previously described[10]. Briefly, for each frame pair, the positions of molecules in the later frame were matched to those in the earlier frame based on a displacement cutoff threshold (R). Typical values of R were set to 5 pixels for fast-moving molecules and 3 pixels for slow-moving molecules (pixel size ~110 nm). The two-dimensional displacements (d) in the x–y plane were calculated for all matched pairs. This procedure was repeated across all frame pairs, and each molecule in the reconstructed image was assigned a displacement value d.

To extract local diffusion coefficients, displacement histograms were generated for all molecules within a defined radius around each central molecule[11]. These histograms were then fitted using a modified isotropic 2D random-walk model:

$$P(r) = 2r/a * exp(-r^2/a) + br, \text{ Equation 1}$$

where r is the single-molecule displacement over the time interval Δt, $a = 4D\Delta t$, and b is a background term accounting for random molecule appearances. This approach has been validated experimentally across different single-molecule densities[10]. The resulting diffusion coefficient D was assigned to the central molecule, and the color in the diffusivity-resolved pc-SM*d*M image reflects this local D value.

Data analysis for density-based single-molecule localization microscope (SMLM) images: For density SMLM image analysis, local molecular density was calculated by counting the number of single molecules within a 30 nm search radius around each target molecule (Figs. 1b, 3i, and 4a). This count was then assigned to the central molecule to generate the density map, producing the color-coded images shown in Figs. 1b and 4a, as well as the molecular density histogram in Fig. 3i.

Monte Carlo simulation of the compartmentalized sliding hopping/CSH Model: For simulation of the CSH model (Fig. 4a), ~50 regions (each 1.5 μm × 1.5 μm) were selected from SMLM images of H2B (chromatin) in ~20 live cells. Density-based SMLM images were generated and subsequently binned into pixelated images with a pixel size of 30 nm. The density of each pixel was computed as the average density of all single molecules within that pixel. To generate spatial masks for sliding regions, an algorithm assigned each pixel a probability of being labeled as a "sliding region" proportional to its local H2B density. The overall fraction of sliding region pixels was defined as the sliding fraction. Diffusion rates were set to 0.2 μm²/s in slow regions (blue) and 2.2 μm²/s in fast regions (red). These values were consistent with the diffusion rates of the slow-diffusing species and fast-diffusing species respectively according to our experiments. A total of 5×10^7 single-molecule trajectories were simulated across the mask. Molecules were initialized at uniformly distributed positions and evolved with a time interval of 6 ms. Each 6 ms interval was subdivided into 100 steps of 0.06 ms. At each step, the molecular position was updated based on the local diffusion coefficient: 0.2 μm²/s in sliding regions and 2.2 μm²/s otherwise. The resulting displacements from all trajectories were used to construct displacement histograms. Two-population fitting was performed to extract the fast diffusion coefficient (D_{fast}) and the fraction of fast-diffusing species (F_{fast}).

Monte Carlo simulation of one-dimensional sliding and intermittent three-dimensional hopping of hOGG1 along a single chromatin fiber: The simulation was conducted within a pool of 10^6-base pairs, with DNA packing densities ranging from 1.6×10^6 bps/μm³ to 5.12×10^7 bps/μm³ (base pairs per μm³), corresponding to 1× to 32× chromatin compaction[32, 50]. The 1D sliding diffusion coefficient was set at 0.58 μm²/s (ref. [5]), while the 3D hopping diffusion coefficient was varied between 1.0 μm²/s and 3.5 μm²/s. The percentage of 8-oxo-G lesions was set between 1 per 10^5 to 1 per 10^3 base pairs[51]. hOGG1 was initially placed at random positions along the DNA sequence. Each simulation step represented a 10 ms interval, during which the enzyme performed sliding and hopping. For a given sliding fraction F(slide), hOGG1 slided

along DNA for F(slide)×10 ms and underwent 3D diffusion for (1–F(slide))×10 ms. Only 8-oxo-G sites encountered during 1D sliding were considered repairable (Fig. 4b). The number of DNA bases skipped during 3D diffusion was estimated as the product of DNA packing density and the volume explored during the hopping step. The search process concluded once all 8-oxo-G lesions had been detected. The repair rate (in base pairs per second) was calculated as the total number of 8-oxo-G sites divided by the total time spent in both sliding and hopping. For each condition, simulations were repeated ~100 times, and the average repair rates were plotted in Figs. 4c to 4f.

Quantification of 8-oxo-G clusters in fixed cells: Clustering analysis was performed by density-based spatial clustering of applications with noise (DBSCAN). The algorithm uses two user-selectable parameters, the search radius and the minimal point of single-molecule localizations within that radius, to identify clusters with dense single molecules. For localizing the 8-oxo-G clusters in the nucleus, we used 30 nm as the search radius, and less than 12 points (within the 30 nm search radius) were excluded during the analysis.

Acknowledgments: L.X. and S. J. acknowledges financial supports from National Key R&D Program of China (2022YFA1305400), National Natural Science Foundation of China (22274122, 22104113), Fundamental Research Funds for the Central Universities interdisciplinary (2042023kf1012), and Innovative Talents Foundation from Renmin Hospital of Wuhan University (JCRCFZ-2022-010). S. J. acknowledges financial support from National Natural Science Foundation of China (22302092).

Author contributions:

Conceptualization: L. X., J. Z. Methodology: L. X., J. Z., K. X., Z. Z., L. Z.Investigation: J. Z., J. D.Visualization: L. X., J. Z.Project administration: L. X.Supervision: L. X., K. X., G. L., M. Y., L. Z., Q.Y., W. H., S. J.Writing-original draft: L. X., J. Z.Writing-review & editing: K. X.

Competing interests: Authors declare that they have no competing interests.

Materials & Correspondence: Correspondence and requests for materials should be addressed to L.X.

Diversity, equity, ethics, and inclusion: All collaborators of this study have fulfilled the criteria for authorship required by Nature Publish Group journals have been included as authors, as their participation was essential for the design and implementation of the study. Roles and responsibilities were agreed among collaborators ahead of the research.

Data availability: The codes used for the simulations are available at:

https://github.com/paldream89/hOGG1_simulation. The data that support the findings of this study are available from the corresponding author upon reasonable request.

Supplemental information

Supplementary Information: Extended Data Figs. 1-6

References:

1. Zhou, H.-X., Rivas, G. & Minton, A.P. Macromolecular Crowding and Confinement: Biochemical, Biophysical, and Potential Physiological Consequences. *Annu. Rev. Biophys.* **37**, 375-397 (2008).
2. Nagy, Z. & Soutoglou, E. DNA repair: easy to visualize, difficult to elucidate. *Trends Cell Biol.* **19**, 617-629 (2009).
3. Friedman, J.I. & Stivers, J.T. Detection of Damaged DNA Bases by DNA Glycosylase Enzymes. *Biochemistry* **49**, 4957-4967 (2010).
4. Esadze, A. & Stivers, J.T. Facilitated Diffusion Mechanisms in DNA Base Excision Repair and Transcriptional Activation. *Chem. Rev.* **118**, 11298-11323 (2018).
5. Blainey, P.C., van Oijen, A.M., Banerjee, A., Verdine, G.L. & Xie, X.S. A base-excision DNA-repair protein finds intrahelical lesion bases by fast sliding in contact with DNA. *Proc. Natl. Acad. Sci.* **103**, 5752-5757 (2006).
6. Vestergaard, C.L., Blainey, P.C. & Flyvbjerg, H. Single-particle trajectories reveal two-state diffusion-kinetics of hOGG1 proteins on DNA. *Nucleic Acids Res.* **46**, 2446-2458 (2018).
7. Rowland, M.M., Schonhoft, J.D., McKibbin, P.L., David, S.S. & Stivers, J.T. Microscopic mechanism of DNA damage searching by hOGG1. *Nucleic Acids Res.* **42**, 9295-9303 (2014).
8. Hansen, A.S., Amitai, A., Cattoglio, C., Tjian, R. & Darzacq, X. Guided nuclear exploration increases CTCF target search efficiency. *Nat. Chem. Biol.* **16**, 257-266 (2020).
9. Mazzocca, M. *et al.* Chromatin organization drives the search mechanism of nuclear factors. *Nat. Commun.* **14**, 6433 (2023).

10. Xiang, L., Chen, K., Yan, R., Li, W. & Xu, K. Single-molecule displacement mapping unveils nanoscale heterogeneities in intracellular diffusivity. *Nat. Methods* **17**, 524-530 (2020).
11. Han, C. *et al.* Super-Resolution Diffusivity Mapping Reveals Spatial Correlations Between Lateral Mobility and Structural Heterogeneities on Cellular Membranes. *bioRxiv*, 2025.2004.2001.646704 (2025).
12. Li, W. & Xu, K. Super-Resolution Mapping and Quantification of Molecular Diffusion via Single-Molecule Displacement/Diffusivity Mapping (SMdM). *Acc. Chem. Res.* **58**, 1224-1235 (2025).
13. Zhang, M. *et al.* Rational design of true monomeric and bright photoactivatable fluorescent proteins. *Nat. Methods* **9**, 727 (2012).
14. He, C., Wu, C.Y., Li, W. & Xu, K. Multidimensional Super-Resolution Microscopy Unveils Nanoscale Surface Aggregates in the Aging of FUS Condensates. *J. Am. Chem. Soc.* **145**, 24240-24248 (2023).
15. Stone, M.B. & Veatch, S.L. Steady-state cross-correlations for live two-colour super-resolution localization data sets. *Nat. Commun.* **6**, 7347 (2015).
16. Engl, W. *et al.* Single-molecule imaging of SWI/SNF chromatin remodelers reveals bromodomain-mediated and cancer-mutants-specific landscape of multi-modal DNA-binding dynamics. *Nat. Commun.* **15**, 7646 (2024).
17. Campalans, A., Amouroux, R., Bravard, A., Epe, B. & Radicella, J.P. UVA irradiation induces relocalisation of the DNA repair protein hOGG1 to nuclear speckles. *J. Cell Sci.* **120**, 23-32 (2007).
18. Choi, A.A., Zhou, C.Y., Tabo, A., Heald, R. & Xu, K. Single-molecule diffusivity quantification in Xenopus egg extracts elucidates physicochemical properties of the cytoplasm. *Proc. Natl. Acad. Sci.* **121**, e2411402121 (2024).
19. Choi, A.A. & Xu, K. Single-Molecule Diffusivity Quantification Unveils Ubiquitous Net Charge-Driven Protein–Protein Interaction. *J. Am. Chem. Soc.* **146**, 10973-10978 (2024).
20. Lafontaine, D.L.J., Riback, J.A., Bascetin, R. & Brangwynne, C.P. The nucleolus as a multiphase liquid condensate. *Nat. Rev. Mol. Cell Bio.* **22**, 165-182 (2021).
21. Cremer, T. & Cremer, C. Chromosome territories, nuclear architecture and gene regulation in mammalian cells. *Nat. Rev. Genet.* **2**, 292-301 (2001).
22. Cremer, T. *et al.* The Interchromatin Compartment Participates in the Structural and Functional Organization of the Cell Nucleus. *Bioessays* **42**, e1900132 (2020).
23. Michel, M. *et al.* Small-molecule activation of OGG1 increases oxidative DNA damage repair by gaining a new function. *Science* **376**, 1471-1476 (2022).
24. Janssen, A., Colmenares, S.U. & Karpen, G.H. Heterochromatin: Guardian of the Genome. *Annu. Rev. Cell Dev. Biol.* **34**, 265-288 (2018).
25. Allshire, R.C. & Madhani, H.D. Ten principles of heterochromatin formation and function. *Nat. Rev. Mol. Cell Bio.* **19**, 229-244 (2018).
26. Chiolo, I. *et al.* Double-Strand Breaks in Heterochromatin Move Outside of a Dynamic HP1a Domain to Complete Recombinational Repair. *Cell* **144**, 732-744 (2011).
27. Ryu, T. *et al.* Heterochromatic breaks move to the nuclear periphery to continue recombinational repair. *Nat. Cell Biol.* **17**, 1401-1411 (2015).
28. Hanna, B.M.F., Helleday, T. & Mortusewicz, O. OGG1 Inhibitor TH5487 Alters OGG1 Chromatin Dynamics and Prevents Incisions. *biomolecules* **10**, 1483 (2020).
29. Hammar, P. *et al.* The lac Repressor Displays Facilitated Diffusion in Living Cells. *Science* **336**, 1595-1598 (2012).

30. Song, F. *et al.* Cryo-EM Study of the Chromatin Fiber Reveals a Double Helix Twisted by Tetranucleosomal Units. *Science* **344**, 376-380 (2014).
31. Mirny, L. *et al.* How a protein searches for its site on DNA: the mechanism of facilitated diffusion. *J. Phys. A Math. Theor.* **42**, 434013 (2009).
32. Woodcock, C.L. & Ghosh, R.P. Physical and data structure of 3D genome. *Sci. Adv.* **2** (2010).
33. Bruner, S.D., Norman, D.P.G. & Verdine, G.L. Structural basis for recognition and repair of the endogenous mutagen 8-oxoguanine in DNA. *Nature* **403**, 859-866 (2000).
34. Nash, H.M., Lu, R., Lane, W.S. & Verdinel, G.L. The critical active-site amine of the human 8-oxoguanine DNA glycosylase, hOgg1: direct identification, ablation and chemical reconstitution. *Chem. Biol.* **4**, 693-702 (1997).
35. Shigdel, U.K. *et al.* The trajectory of intrahelical lesion recognition and extrusion by the human 8-oxoguanine DNA glycosylase. *Nature Communications* **11**, 4437 (2020).
36. van der Kemp, P.A., Charbonnier, J.B., Audebert, M. & Boiteux, S. Catalytic and DNA-binding properties of the human Ogg1 DNA N-glycosylase/AP lyase: biochemical exploration of H270, Q315 and F319, three amino acids of the 8-oxoguanine-binding pocket. *Nucleic Acids Res.* **32**, 570-578 (2004).
37. Sakonsinsiri, C. *et al.* Aptamer-based colorimetric detection of the DNA damage marker 8-oxo-dG using cysteamine-stabilised gold nanoparticles. *RSC Adv.* **12**, 25478-25486 (2022).
38. Hu, H. *et al.* Highly-sensitive and homogenous detection of 8-oxoguanine based DNA oxidative damage by a CRISPR-enhanced structure-switching aptamer assay. *Biosens. Bioelectron.* **239**, 115588 (2023).
39. Niederauer, C. *et al.* Dual-color DNA-PAINT single-particle tracking enables extended studies of membrane protein interactions. *Nat. Commun.* **14**, 4345 (2023).
40. Jungmann, R. *et al.* Multiplexed 3D cellular super-resolution imaging with DNA-PAINT and Exchange-PAINT. *Nat. Methods* **11**, 313-318 (2014).
41. Liu, N., Dai, M., Saka, S.K. & Yin, P. Super-resolution labelling with Action-PAINT. *Nat. Chem.* **11**, 1001-1008 (2019).
42. Schmidt, J.C., Zaug, A.J. & Cech, T.R. Live Cell Imaging Reveals the Dynamics of Telomerase Recruitment to Telomeres. *Cell* **166**, 1188-1197.e1189 (2016).
43. Chong, S. *et al.* Imaging dynamic and selective low-complexity domain interactions that control gene transcription. *Science* **361**, eaar2555 (2018).
44. Knight, S.C. *et al.* Dynamics of CRISPR-Cas9 genome interrogation in living cells. *Science* **350**, 823 (2015).
45. White, M.D. *et al.* Long-Lived Binding of Sox2 to DNA Predicts Cell Fate in the Four-Cell Mouse Embryo. *Cell* **165**, 75-87 (2016).
46. Holehouse, A.S. & Kragelund, B.B. The molecular basis for cellular function of intrinsically disordered protein regions. *Nat. Rev. Mol. Cell Bio.* **25**, 187-211 (2024).
47. Bremer, A. *et al.* Deciphering how naturally occurring sequence features impact the phase behaviours of disordered prion-like domains. *Nat. Chem.* **14**, 196-207 (2022).
48. Folkmann, A.W., Putnam, A., Lee, C.F. & Seydoux, G. Regulation of biomolecular condensates by interfacial protein clusters. *Science* **373**, 1218-1224 (2021).
49. Schaich, M.A., Weaver, T.M., Roginskaya, V., Freudenthal, B.D. & Van Houten, B. Single-molecule analysis of purified proteins and nuclear extracts: Insights from 8-oxoguanine glycosylase 1. *DNA Repair* **134**, 103625 (2024).

50. Phillips, R., Kondev, J., Theriot, J., & Garcia, H. *Physical Biology of the Cell*, Edn. 2nd. (Garland Science, Taylor & Francisco Group, LLC, New York; 2012).
51. Shigenaga, M.K., Park, J.-W., Cundy, K.C., Gimeno, C.J. & Ames, B.N. In Vivo Oxidative DNA damage: Measurement of 8-Hydroxy-2′-deoxyguanosine in DNA and urine by high-performance liquid chromatography with electrochemical detection, in *Meth. Enzymol.*, Vol. 186 521-530 (Academic Press, 1990).

Supplementary Files

This is a list of supplementary files associated with this preprint. Click to download.

- SINatureChem.pdf